Article

Biosensing with Surface-Charge-Modulated Graphene Field-Effect Transistors beyond Nonlinear Electrolytic Screening

Shota Ushiba,* Tomomi Nakano, Ayumi Shinagawa, Naruto Miyakawa, Tadashi Kato, Katsuyuki Yofu, Takao Ono, Yasushi Kanai, Shinsuke Tani, Masahiko Kimura, and Kazuhiko Matsumoto

Read Online

ACCESS | Metrics & More | Article Recommendations | Supporting Information

ABSTRACT: In field-effect transistor (FET) biosensors, charge screening in electrolyte solutions limits the sensitivity, thereby restricting the applicability of FET sensors. This is particularly pronounced in graphene FET (GFET) biosensors, where the bare graphene surface possesses a strongly negative charge, which impedes the high sensitivity of GFETs owing to nonlinear electrolytic screening at the interfaces between graphene and liquid. In this study, we counteracted the negative surface charge of graphene by decorating positively charged compounds and demonstrated the sensing of C-reactive protein (CRP) with surface-charge-modulated GFETs (SCM-GFETs). We integrated multiple SCM-GFETs with anti-CRP antibodies and nonfunctionalized GFETs into a chip and measured differentials to eliminate background changes to improve measurement reliability. The FET response corresponded to the fluorescence images, which visualized the specific adsorption of CRP. The estimated dissociation constant was consistent with previously reported values; this supports the conclusion that the results are attributed to specific adsorption. Conversely, the signal in GFETs without decoration was obscured by noise because of nonlinear electrolytic screening, further emphasizing the significance of surface-charge modulation. The limit of detection of the system was determined to be 2.9 nM. This value has the potential to be improved through further optimization of the surface charges to align with specific applications. Our devices effectively circumvent nonlinear electrolytic screening, opening the door for further advancements in GFET biosensor technology.
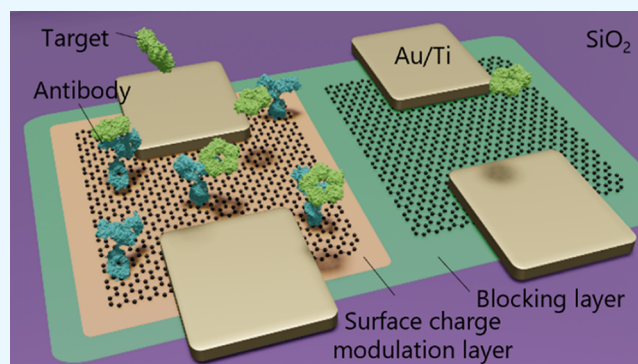
1. INTRODUCTION

In field-effect transistor (FET) biosensors, the interfaces between solid and liquid are crucial as sensors detect changes in the surface potential (ψ_0) by analyte charges. Some of these charges are screened by ions in electrolyte solutions; thus, only a fraction of the charges induce opposite charges in the FET. Electrolytic screening is commonly described by the Debye−Hückel (DH) model based on the Poisson−Boltzmann theory. However, the DH model is only valid when ψ_0 is smaller than $\psi_L = |k_B T/ze|$, where e is the elementary charge and z is the valency of the bulk electrolyte;[1] for example, $\psi_L = 26$ mV for monovalent electrolyte solutions. When ψ_0 exceeds ψ_L, the DH model becomes less precise, and the excess charge density in the electrical double layer (EDL) varies nonlinearly with ψ_0, resulting in enhanced charge screening, known as nonlinear screening.[2,3] This is evident from eq 1,[3,4] which represents the FET sensitivity toward the binding analyte charge (σ_{ana}).

$$\frac{d\psi_0}{d\sigma_{ana}} \sim \frac{1}{\cosh\left(\frac{ze\psi_0}{2k_B T}\right)} \tag{1}$$

The highest sensitivity is achieved when ψ_0 approaches zero (an uncharged surface). Conversely, the sensitivity decreases as ψ_0 increases (or decreases), and it eventually becomes zero when ψ_0 becomes much larger (or smaller). This is a serious problem for biosensing because the FET sensors will not respond to the charged analytes. Therefore, it is imperative to engineer ψ_0 and surface charge in FET biosensors. There have been several reports on engineering ψ_0 and surface charges in FET biosensors to improve their sensitivity. Shoorideh et al. modified the surface charge at the solid/liquid interface of a Si FET using both front and back gate.[5] More recently, Gupta et al. modulated the negatively charged SiO_2 surface of Si FETs by depositing positively charged blocking molecules, improving sensitivity by 51%.[3]
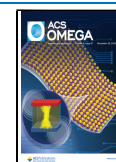
Among the various types of FET biosensors, graphene FET (GFET) biosensors have attracted particular attention owing to their extremely high electron/hole mobilities[6,7] and their two-dimensional (2D) nature,[8,9] which provide a highly sensitive 2D sensing platform. Numerous studies have reported the ability of GFET biosensors to detect biomolecules, including proteins,[10] small antigens,[11] exosomes,[12] and viruses.[13] However, relatively less emphasis has been placed on the engineering of ψ_0 and surface charge in GFET biosensors. In this study, we modified the surface charge of graphene and demonstrated biosensing using surface-charge-modulated GFETs (SCM-GFETs) to enhance sensitivity. Many studies have indicated that the graphene surface is negatively charged. For instance, Bepete et al. showed that the ζ-potential of graphene was $\zeta = -45$ mV under neutral pH conditions.[14] Zuccaro et al. reported that the isoelectric point (pI) of unmodified graphene was less than 3.3, indicating that graphene is negatively charged at neutral pH conditions.[15] Negative charges on graphitic particles were also observed in other studies.[16] The negative charge of graphene primarily arises from the structure and the water molecules at the EDL and specific adsorption of OH^- ions.[15] Although the value of the ζ-potential of graphene may fluctuate depending on the fabrication process and substrates present underneath the graphene,[15] these studies imply that signals of GFETs without surface-charge modulation may be hindered by nonlinear electrolytic screening; thus, counterbalancing the surface charge of graphene is deemed essential in GFET biosensors. The negatively charged graphene surface can be altered by decoration with positively charged molecules. For example, Zuccaro et al. showed that the value of pI increased by up to 7.5 through consecutive electrochemical modification using 4-aminobenzylamine.[15]

To modify the surface charge, we employed quaternary ammonium compounds (QACs) in an NR_3^+ polystyrene (PS) bead suspension, where both free QACs and QACs modified on the beads were included, with a ζ-potential of 1.8 mV. GFET biosensors specifically detect the target analyte by depositing the QACs in conjunction with a capture probe. It is noted that FET sensors respond not only to analyte charges but also to environmental variations such as ionic strength, pH, and temperature changes. These changes may result in baseline drift, making it challenging to analyze the sensor response.[17,18] We integrated nonfunctionalized GFETs next to the capture probe functionalized GFETs and performed differential measurements to cancel the response to background changes and extract net signals of the target. Additionally, as GFET characteristics suffer from FET-to-FET variability due to process variations, we integrated multiple GFETs into the chips and calculated the average values of the GFET characteristics to improve the measurement reliability. Furthermore, target molecules that were fluorescently labeled on the devices were visualized after electrical measurements using a fluorescence microscope. We verified that the obtained GFET signal was a result of specific adsorption of the target onto the antibodies.

2. EXPERIMENTAL SECTION

2.1. Materials. Graphene films were purchased from Graphene Platform. Human recombinant C-reactive protein (CRP) and antihuman CRP monoclonal antibody (anti-CRP mAb) (304-51283, clone 12D-2C-36) were obtained from FUJIFILM Wako. CRP was fluorescently labeled using an

Alexa Fluor 488 NHS Ester (Thermo Fisher Scientific) to be used as the target molecule in this study. Bovine serum albumin (BSA) was purchased from Sigma−Aldrich (St. Louis, MO, USA). Dulbecco's phosphate-buffered saline (D-PBS(−)) was purchased from Nacalai Tesque. PBS was diluted with deionized water to obtain 0.01 × PBS. NR_3^+ ($d = 1$ μm, 01-05-103) and COOH PS bead ($d = 1$ μm, 01-02-103) suspensions were purchased from Micromod. In the NR_3^+ PS bead suspension, free QACs, i.e., detached from the bead surface, were included based on the mass spectrometry. Anti-influenza B virus nucleoprotein (anti-NP) mAb (BMRib010, clone FLB-1653) was purchased from BioMatrix Research.

2.2. Fluorescence Labeling of CRP. The Alexa Fluor 488 NHS Ester was dissolved in dimethylformamide at 10 mg/mL. The reactive dye solution was added to CRP of 9.5 μM in 0.01 × PBS and incubated for 1 h at room temperature with stirring. Following the reaction, the conjugate was separated from the unreacted labeling reagent using PD MiniTrap G-25 columns (GE Healthcare). The resultant concentration of labeled CRP was 7.8 μM, with a degree of labeling of 2.5. The binding affinity between the labeled CRP and the anti-CRP mAb in 0.01 × PBS was confirmed through biolayer interferometry (Figure S1), demonstrating that the labeling and the low ionic strength did not interrupt their interactions. This result aligns with the previous report.[25]

2.3. ζ-Potential Measurements. ζ-potential was measured using a Zetasizer Nano ZS90 (Malvern Panalytical) instrument. The ζ-potentials of NR_3^+ and COOH PS bead suspensions in 0.01 × PBS were measured as 1.8 and −47.2 mV, respectively. The ζ-potentials of CRP, anti-CRP mAb, anti-NP mAb, and BSA were −40, −24, −14, and −29 mV, respectively. The ζ-potential of the mixture of the NR_3^+ PS bead suspension and the anti-CRP mAb was −4.6 mV, which is an intermediate value between those of the NR_3^+ PS bead suspension and the anti-CRP mAb.

2.4. Fabrication of GFET Arrays. The devices were fabricated as follows. The process is also described elsewhere.[19,20] The GFETs were fabricated by transferring CVD-graphene onto a Si/SiO_2 substrate with a thickness of 525 μm/290 nm via etching of the underlying copper foil. The source/drain electrode lines were formed with 10 nm Ti and 90 nm Au using electron-beam evaporation. The graphene films were patterned into an array of six rows and nine columns using a 300×300 μm^2 mask via oxygen plasma etching, resulting in 54 GFETs (#1−#54) integrated into the chips. An optical image of a typical GFET is presented in Figure 1a. The channel width and length of each GFET were 100 μm. It was confirmed that the graphene films were not torn or contaminated using an optical microscope (DSX510, Olympus) and a deep-learning method.[20] The GFET array was divided into two regions (Region 1: no. 1−24 and Region 2: no. 31−54) using a silicone rubber placed on the chip. The GFETs (#25−#30) were covered with rubber and thus were not used for analysis. The rubber was also used as a reservoir.

2.5. Immobilization of QACs, Anti-CRP mAb, and BSA Blocking. NR_3^+ PS bead suspension (5.0 mg/mL) in 0.01 × PBS was mixed with anti-CRP mAb (7.6 μM) (or anti-NP mAb (6.6 μM)) in 0.01 × PBS in a 1:1 volume ratio. Anti-CRP mAb was bound to the beads in the prepared solution. The solution also contained unbound anti-CRP mAb. As the GFET array was divided into two regions by silicone rubber, the two regions were individually functionalized. The mixed solution was dropped onto Region 1 and incubated for 0.5 h at room
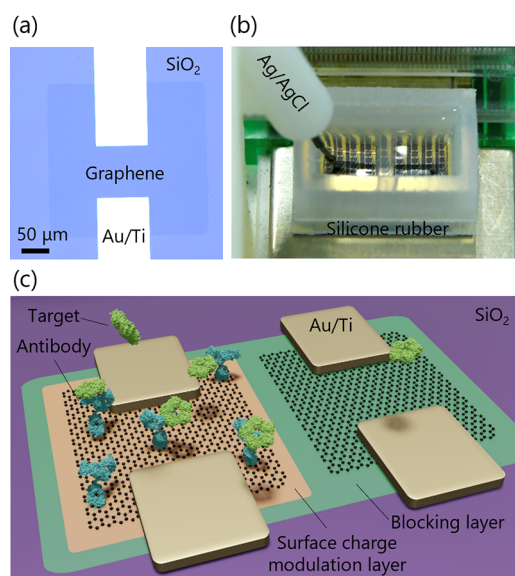
Figure 1. (a) Optical image of a typical graphene field-effect transistor (GFET). (b) Photo of the device set on the custom-built portable measurement system. (c) Schematic of the device representing the surface-charge-modulated GFET (SCM-GFET) with capture probes (GFET$_{sig}$, left) and the reference GFET (GFET$_{ref}$, right).

temperature. Through this process, QACs and mAb were decorated on the GFETs. Region 2 was incubated with 0.01× PBS, which was not functionalized. After incubation, both regions were washed with 0.01× PBS and subsequently treated with 1% BSA in 0.01 × PBS for 0.5 h to block nonspecific adsorption. After washing, the chip was ready for biosensing. The GFETs in Region 1, where the mAb was immobilized, are referred to as GFETs$_{sig}$, and those in Region 2, where no mAb was immobilized, are referred to as GFETs$_{ref}$. These can be flipped if the mAb is immobilized in Region 2. The height of the inner wall between Regions 1 and 2 was lower than that of the outer wall. Therefore, it is possible to share (not to share) a solution between two separated regions by raising (lowering) the solution surface. Consequently, solutions remained segregated during the immobilization process, whereas they were intermixed during the electrical measurements.

2.6. Portable Measurement Equipment. The measurement system is depicted in Figure S2, comprising a personal computer (PC), microcontroller, and custom-designed printed circuit board (PCB). The PC is responsible for recording and processing the measured data as well as programming the microcontroller with Python. The microcontroller supplies power to the PCB and generates digital control signals. Equipped with 14-bit digital-to-analog (DAC) outputs, the microcontroller controls the drain−source bias V_{DS} and gate−source voltage V_{GS}. The custom-designed PCB forwards the generated V_{DS} and V_{GS} biases to the GFET array. The resulting drain−source current I_{DS} for each GFET and leakage-current I_{GS} are then routed from the PCB to current−voltage converters and 16-bit analog-to-digital converters (ADC) on the microcontroller. All data are subsequently transmitted back to the PC via USB. The dimensions of the equipment are as follows: length 125 mm, width 85 mm, height 45 mm, with a weight of 220 g.

2.7. Electrical Measurements. The devices were characterized using custom-built portable measurement systems (Figures 1b and S2). A buffer solution of 0.01 ×

PBS was used for the electrical measurements. A V_{DS} bias of 0.1 V was applied, and a V_{GS} bias was imposed through the solution via a Ag/AgCl electrode. The I_{DS} was measured while sweeping V_{GS}. V_{GS} at the minimum conductance point (V_{DP}), also known as the charge neutrality point, was calculated for each GFET by using polynomial fitting. The equivalent I_{GS} value for each G-FET was estimated to be <1 μA, which was much smaller than I_{DS}.

2.8. Target Sensing Protocol. Prior to target sensing, initial measurements were conducted in 0.01 × PBS for 0.5 h. The measurement buffer solution was then swapped with the target solution and incubated at room temperature for 0.5 h, which is sufficient for reaching equilibrium based on the binding kinetics in Figure S1. The device remained floating during the incubation step; thus, no electrical measurements were performed during the period. Following incubation, the device was rinsed with 0.01 × PBS to remove unbound protein. The electrical measurements were then carried out in the measurement buffer solution for 0.5 h (or 40 min for the experiment in Figure 2). This process was repeated until the
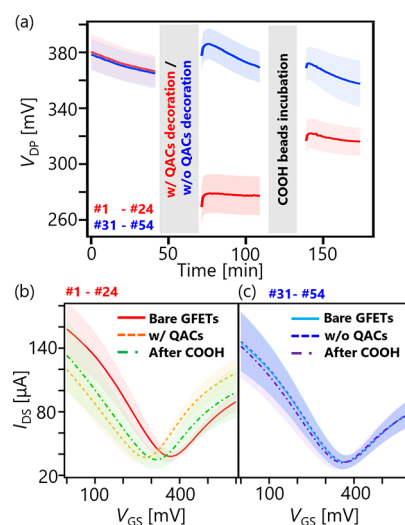

Figure 2. (a) Time series of the mean V_{DP} for the GFETs in Region 1 (#1−#24, red) and the GFETs in Region 2 (#31−#54, blue). The GFETs in Region 1 were decorated with the quaternary ammonium compounds (QACs) and subsequently, COOH beads were incubated; the GFETs in Region 2 were not decorated, and subsequently, COOH beads were incubated. Red and blue lines correspond to GFETs in Regions 1 and 2, respectively. (b,c) Mean I_{DS}−V_{GS} transfer curves correspond to the end-points of bare GFETs (solid line), those after the decoration process (dashed line), and those after COOH beads incubation (dash-dotted line). The shadows represent standard deviations.

target concentration reached a certain value (38 nM for Figures 3 and 5 and 76 nM for Figure 4). The response of a blank sample, that is, a target concentration of 0 nM, was measured several times to confirm that the response to the solution exchange process was smaller than that to the target signals.

2.9. Data Analysis. As multiple GFETs$_{sig}$ and GFETs$_{ref}$ were integrated on the chips, the output of the differential measurement ΔV_{DP} was considered to be the difference between the group means. We used Bayesian estimation to calculate ΔV_{DP} for the two groups with credible intervals. By assuming that the obtained V_{DP} followed normal distributions
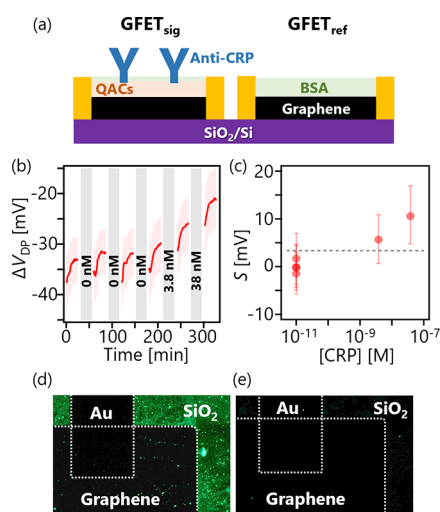
Figure 3. (a) Schematic of GFET$_{sig}$ (#1−#24), where the surface was decorated with the QACs, anti-CRP monoclonal antibody (mAb), and BSA, and GFET$_{ref}$ (#31−#54), where the surface was decorated with BSA blocking. (b) Time series of the mean ΔV_{DP}. The red shadow represents 95% of Bayesian credible intervals. Blank samples were measured three times, and then, the concentration of CRP was increased to 38 nM. (c) Signal (S) as a function of CRP concentration. The error bar represents 95% Bayesian credible intervals. The dashed line represents the noise floor ($3\sigma_N$ = 3.3 mV). (d,e) Typical fluorescence images of GFET$_{sig}$ (d) and GFET$_{ref}$ (e), respectively. Scale bars are 50 μm.
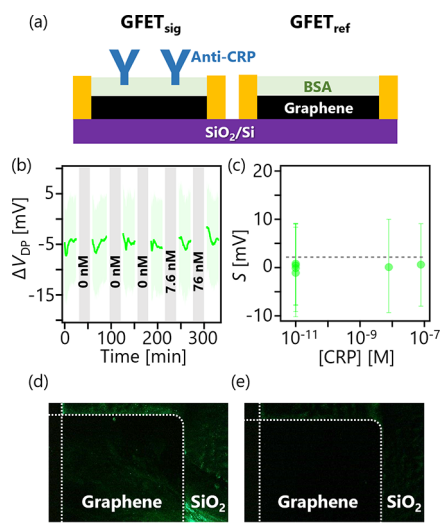

Figure 4. (a) Schematic of GFET$_{sig}$ (#31−#54), where the surface was decorated with anti-CRP mAb, and BSA, and GFET$_{ref}$ (#1−#24), where the surface was decorated with BSA. In this configuration, the surface charge was not modulated by the QACs. (b) Time series of the mean ΔV_{DP}. The blue shadow represents 95% Bayesian credible intervals. Blank samples were measured three times, and then the concentration of CRP was increased to 76 nM. (c) Signal (S) as a function of CRP concentration. The error bar represents 95% Bayesian credible intervals. The dashed line represents the noise floor ($3\sigma_N$ = 2.2 mV). (d,e) Typical fluorescence images of GFET$_{sig}$ (d) and GFET$_{ref}$ (e). Scale bars are 50 μm.

$(V_{DP, D} \sim N(\mu_D, \sigma_D^2)$, where μ and σ are the mean and standard deviation and the subscript D is sig or ref, the posterior distributions of $(\mu_{sig}, \sigma_{sig})$ and $(\mu_{ref}, \sigma_{ref})$ were inferred by using Markov chain Monte Carlo (MCMC)

methods.[21] From the MCMC sample, we examined the credible difference of means ($\Delta V_{DP} = \mu_{sig} - \mu_{ref}$). The discrepancy between the GFETs$_{sig}$ and GFETs$_{ref}$ structures resulted in nonzero values of ΔV_{DP}. Therefore, the offset voltage was subtracted to calculate the net signal (S). The offset voltage was determined as the mean value of ΔV_{DP} based on blank sample measurements ($\Delta V_{DP, 0 nM}$). Thus, S is given by $S = \Delta V_{DP} - \Delta V_{DP, 0 nM}$. The noise floor was defined as $3\sigma_N$, where σ_N is the standard deviation of S for the blank samples. To plot S as a function of the target concentration in a semilog plot, a base concentration of 10 pM was added, which was below the measured target concentration.

2.10. Fluorescence Microscopy Assay. To verify the specific adsorption of fluorescently labeled CRP on anti-CRP mAb-functionalized GFETs, fluorescence images were taken after the electrical measurements using a fluorescence microscope (ECLIPSE LV100N POL, Nikon) equipped with a 50× objective lens (TU Plan Fluor, NA 0.8, Nikon). Images were captured at an exposure time of 1 s.

3. RESULTS AND DISCUSSION

3.1. Concept of SCM-GFET Biosensors. Figure 1c illustrates our device, which comprises two configurations of GFETs: one is a sensing GFET (GFET$_{sig}$), where the surface was decorated with QACs and capture probes, and the other was a reference GFET (GFET$_{ref}$), which was used to record the background as it did not possess capture probes. Due to variations in the fabrication process, the values of $V_{DP,sig}$ and $V_{DP,ref}$ were diverse as shown in Figure S3; thus, we computed their means (μ_{sig} and μ_{ref}) to enhance the measurement reliability. Background changes, such as variations in the ionic strength, pH, and temperature of the buffer solution, were eliminated through differential measurements ($\Delta V_{DP} = \mu_{sig} - \mu_{ref}$). The implementation of a positively charged compound to counteract the negative potential of graphene ($\zeta = -45$ mV[14]) enables the devices to effectively overcome a strong nonlinear electrolytic screening.

3.2. COOH PS-Bead Sensing by SCM-GFETs. To validate the concept of the SCM-GFETs, we first performed a fundamental experiment using negatively charged COOH PS beads ($\zeta = -47.2$ mV). Figure 2a shows the time series of the mean V_{DP} for GFETs in Region 1 (red) and GFETs in Region 2 (blue). During the initial measurements (until 40 min; Figure 2a), the GFETs in both regions were not functionalized, i.e., bare surfaces. Therefore, the V_{DP} values as well as $I_{DS}-V_{GS}$ transfer curves were almost superimposed on each other (Figure 2a−c).

After the initial measurements, the surface charges of the GFETs in Region 1 were modulated by the NR$_3^+$ PS bead suspension including free QACs and QACs on the beads, whereas those in Region 2 were not. Following the rinse process, the physisorption of the PS beads in Region 1 was observed by using optical microscopy (Figure S4a,b), implying both free QACs and QACs modified on the beads were immobilized. Following, electrical measurements were conducted for 40 min. The corresponding plots in Figure 2a,b show that the values of V_{DP} for the GFETs in Region 1 were shifted down as a result of the surface decoration. This shift is attributed to the positive charge of the quaternary ammonium group, which induces opposite charges in the graphene channel. This result also implies that the ζ-potential of GFETs approached zero by the decoration. In contrast,

those in Region 2 remained relatively unchanged despite a slight drift, as shown in Figure 2a,c.

Subsequently, COOH beads at a concentration of 2.0 mg/mL were incubated in both regions. Electrical measurements were conducted after rinsing. COOH beads were physisorbed onto both regions because of the lack of blocking on the device, as shown in Figure S4c,d, although COOH beads were adsorbed more on the GFETs in Region 1 due to the attractive electrostatic forces. The corresponding plots in Figure 2a,b show that the values of V_{DP} for the GFETs in Region 1 shifted up, which was attributed to the negative charge of COOH. As displayed in Figure S4a, the graphene surface was not entirely covered with the NR_3^+ PS beads but possibly covered with the free QACs. Therefore, the negative charges were potentially present near the graphene surface, resulting in V_{DP} upshifts. In contrast, the values of V_{DP} for the bare GFETs in Region 2 remained relatively unchanged, as shown in Figure 2a,c. The bare GFETs were supposed to respond to the COOH beads because GFETs are recognized as being highly sensitive. Indeed, adsorbed NR_3^+ PS beads in Figure S4a, whose density was almost equivalent to that of COOH beads in Figure S4d, were detected in the bare GFETs. However, in fact, the GFETs did not exhibit a response despite the adsorption of the charged target onto the graphene channel. It is considered that the limited response stems from the strong nonlinear screening caused by the large ψ_0 of the bare graphene. The decoration of the QACs in Region 1 counteracted the large ψ_0, weakening the nonlinear screening and improving the response to the target. These results highlight the significance of modulating the surface charge of GFETs to sense charged analytes.

3.3. CRP Sensing by Anti-CRP mAb-Immobilized SCM-GFETs.

Next, we demonstrated biosensing using the SCM-GFETs. CRP, which is considered a universal biomarker for a variety of diseases, including cardiovascular diseases and disorders, as well as an early indicator of infectious or inflammatory conditions,[22] was used as the target analyte. Figure 3a depicts the schematic of a $GFET_{sig}$ (#1–#24), whose surface was decorated with the QACs, anti-CRP mAb, and BSA blocking, and a $GFET_{ref}$ (#31–#54), whose surface was decorated with BSA blocking alone. The time series of ΔV_{DP} is shown in Figure 3b. The values of ΔV_{DP} drifted, particularly at the onset of the measurements for each step, which remains to be addressed. Nevertheless, the drift was relatively suppressed in the last 10 min at each step (Figure S5). Therefore, the data for the last 10 min of each step were used to calculate S. A plot of S as a function of CRP concentration, presented in Figure 3c, demonstrates a monotonic trend. The standard deviation of S for the blank samples (σ_N) was calculated to be 1.1 mV, resulting in a noise floor ($3\sigma_N$) of 3.3 mV. S surpassed the noise floor at a concentration of 3.8 nM, indicating that there is a significant difference between the signal and noise, and thus, the device responded to the CRP.

To confirm that the GFET signal was responsible for the CRP captured on $GFET_{sig}$, we took fluorescence images after electrical measurements. Figure 3d,e shows typical examples of images of $GFET_{sig}$ and $GFET_{ref}$, respectively. In the $GFET_{sig}$ device, the fluorescence of labeled CRP was observed on both graphene and SiO_2 surface, although the fluorescence on the graphene was partially quenched.[23] As the anti-CRP mAb was immobilized via physisorption, it was present on graphene as well as SiO_2. Therefore, the antigen–antibody reaction occurred on both the graphene and the SiO_2 surface. The fluorescence image in Figure 3d also indicates the location of

the PS beads, which are visible as bright spots. It is noted that fluorescence was also observed apart from the beads. This indicates that the anti-CRP mAbs were also immobilized with the QACs on the device instead of being bound to the beads. These mAbs in proximity to the graphene surface likely contributed to the FET signal. In contrast, the $GFET_{ref}$ device displayed no observable fluorescence on either the graphene or SiO_2 surface; that is, CRP was not adsorbed. Consequently, the results indicate that CRP was specifically adsorbed on $GFET_{sig}$, but not on $GFET_{ref}$, supporting the conclusion that the FET response in Figure 3b,c arose from CRP.

3.4. CRP Sensing by Anti-CRP mAb-Immobilized Non-Surface-Charge-Modulated GFETs.

To demonstrate the crucial role of the surface charge in GFET biosensing, we carried out a control experiment in which CRP sensing was performed without surface-charge modulation. A schematic of the device configuration is depicted in Figure 4a. Figure 4b shows the time series of ΔV_{DP} during the blank sample and the CRP measurements. In contrast to Figure 3b,c, the values of ΔV_{DP} and S in Figure 4b,c remained nearly constant. Notably, S did not surpass the noise floor at a concentration of 76 nM, although it was twice as high as that in Figure 3. Given that S was lower than the noise floor, it was concluded that the device did not respond to CRP in the absence of surface-charge modulation.

It is noteworthy that the fluorescence images in Figures 4d,e and S6 show that CRP was adsorbed on $GFET_{sig}$, but not on $GFET_{ref}$. This suggests that the antigen–antibody reaction occurred on $GFET_{sig}$. Although CRP was less adsorbed in Figure 4d compared to Figure 3d due to repulsive electrostatic forces, the device was supposed to respond against CRP that was still visible in the fluorescence images because GFETs are recognized as highly sensitive sensors. However, as presented in Figure 4c, the FET signal was obscured by the noise. Therefore, it is concluded that the low value of S in Figure 4c was attributed to strong nonlinear electrolytic screening as well as low antigen–antibody reaction efficiency. These results further emphasize the significance of surface-charge modulation of GFETs for biosensing applications.

3.5. CRP Sensing by Anti-NP mAb- and Non-mAb-Immobilized SCM-GFETs.

To further verify that the results in Figure 3 stem from the specific detection of CRP, we conducted another control experiment in which we immobilized anti-NP mAb instead of anti-CRP mAb (Figure 5a). In this configuration, it was expected that CRP would not adsorb onto the device. Figure 5b shows the time series of ΔV_{DP} for the blank samples and CRP measurements. In contrast to Figure 3b,c, the values of ΔV_{DP} and S in Figure 5b,c remained almost constant. S did not surpass the noise floor, even at a concentration of 38 nM, indicating that the device did not respond to the CRP. The fluorescence images taken after the measurements indicated that both $GFET_{sig}$ and $GFET_{ref}$ were devoid of fluorescence, as shown in Figure 5d,e. These findings indicate that nonspecific adsorption was effectively suppressed and aligned with the FET response shown in Figure 5b,c.

As another control experiment, SCM-GFETs with QACs but no anti-CRP mAb were also evaluated (Figure S7a). Similar to Figure 5c, S in Figure S7b remained almost constant even at a concentration of 38 nM, although one point exceeded the noise floor. Since both the anti-NP mAb immobilized- and nonantibody immobilized-SCM-GFETs did not respond to CRP, it can be confidently inferred that the data in Figure 3 are indicative of the specific binding of CRP. We also found that
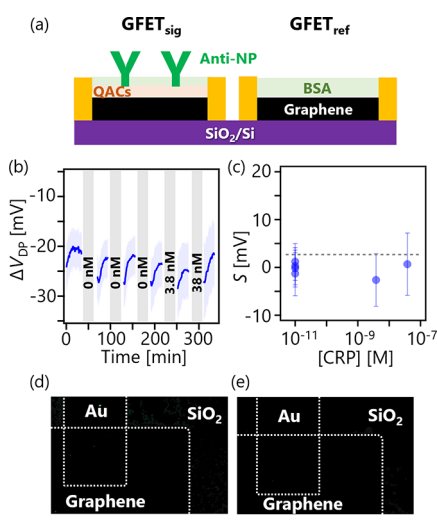
Figure 5. (a) Schematic of $GFET_{sig}$ (#1−#24), where the surface was decorated with the QACs, anti-NP mAb, and BSA, and $GFET_{ref}$ (#31−#54), where the surface was decorated with BSA. (b) Time series of the mean ΔV_{DP}. The blue shadow represents 95% Bayesian credible intervals. Blank samples were measured three times, and then the concentration of CRP was increased to 38 nM. (c) Signal (S) as a function of CRP concentration. The error bars represent 95% Bayesian credible intervals. The dashed line represents the noise floor ($3\sigma_N$ = 2.7 mV). (d,e) Typical fluorescence images of $GFET_{sig}$ (d) and $GFET_{ref}$ (e). Scale bars are 50 μm.

CRP was nonspecifically adsorbed at higher concentrations (Figure S8). This is because the blocking process was not yet fine-tuned, which remains to be addressed.

3.6. Quantitative Evaluation of the Sensitivity of the SCM-GFET Biosensors.
As demonstrated by the results presented in Figures 3−5, the anti-CRP-immobilized SCM-GFETs specifically detected CRP. To assess the sensitivity, we conducted measurements on multiple anti-CRP-immobilized SCM-GFETs, as shown in Figure 3. Multiple anti-NP-immobilized SCM-GFETs were measured for comparison. The results are plotted in Figure 6a,b. The plot in Figure 6a was fitted using eq 2, based on the Langmuir binding model.[24]

$$S = \frac{A[CRP]}{(K_D + [CRP])} + \varepsilon, \quad \varepsilon \sim N(0, \sigma_{obs}) \quad (2)$$
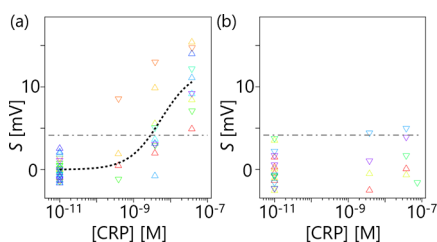

Figure 6. (a,b) S as a function of CRP concentration of anti-CRP mAb-immobilized SCM-GFETs (a) and anti-NP mAb-immobilized SCM-GFETs (b). Each color corresponds to different devices, and the results for 12 devices are plotted in (a) and those for 5 devices are plotted in (b). The upper triangles represent the device configuration of $GFETs_{sig}$ (#1−#24) and $GFETs_{ref}$ (#31−#54), and the lower triangles represent that of $GFETs_{sig}$ (#31−#54) and $GFETs_{ref}$ (#1−#24). The dashed line in (a) is a fitting curve based on the Langmuir binding model. The dashed-dotted line represents the noise floor.

where A, K_D, ε, and σ_{obs} represent the intensity, dissociation constant, observation noise, and standard deviation, respectively. From the fitting by using the MCMC method, mean K_D and 95% Bayesian credible intervals were estimated to be 5.5 and (2.1 and 13.8 nM), respectively. The value of K_D is similar to previously reported values.[25] This coincidence further supports the specific detection of the CRP and anti-CRP mAb reactions by the devices. The noise floor, defined as three times the standard deviation of S for 0 nM, was calculated to be 4.2 mV. The intersection of the noise floor and mean fitting curve yields the limit of detection (LOD) in the system, which was determined to be 2.9 nM. This value was smaller than the CRP concentration in the plasma of healthy individuals (6.8 nM),[25] suggesting the practical applicability of our devices. The plot also shows a consistent trend regardless of the functionalized regions of the mAb: $GFETs_{sig}$ (#1−#24) and $GFETs_{sig}$ (#31−#54). This result suggests that the measurement system was robust, although the response intensity varied between devices, probably due to variations in the FET fabrication and functionalization processes. Conversely, the plot in Figure 6b shows that the overall results were buried by the noise, although a few points barely surpassed the noise floor. This result again supports the fact that the anti-CRP-immobilized SCM-GFETs specifically detected CRP.

4. DISCUSSION

The results in Figures 2−6 provide strong evidence that the surface charge was altered by decoration by the quaternary ammonium cation included in the PS bead suspension. We considered that free QACs played a significant role for the sensing but the QACs on the beads did not. This is because the diameter of the beads was 1 μm, which is much larger than the screening length. Therefore, the CRP in proximity to the graphene surface was detected but CRP adsorbed on the beads would not. To substantiate this hypothesis, the correlation between the amount of the adsorbed beads and the response intensity against CRP of 38 nM was investigated after the experiment in Figure 3. Figure S9 shows no apparent correlation between the amount of adsorbed beads and the response intensity, implying that PS beads had a small or negligible impact on biosensing, while emphasizing the significance of the free QACs adsorbed on the graphene surface. In the current process, decoration and mAb immobilization were not uniform, as indicated by the fluorescence image in Figure 3d. This inhomogeneity may account for the variations in the response intensity of $GFET_{sig}$ over the array. Therefore, it is important to integrate multiple GFETs on the chips and calculate the average values to improve the measurement reliability. Although there is a potential for the improvements, the presented data demonstrates the proof-of-concept of the surface-charge-modulated GFETs.

The reason why the quaternary ammonium cation was used in this study as a positively charged material is because of its unchanging valence in response to pH changes.[26] As other positively charged compounds, poly-L-lysine (PLL) may also be considered due to its strong positive charge at neutral pH conditions,[27] and its widespread use in bioassay and biosensing.[28,29] However, unlike the quaternary ammonium cation, the ζ-potential of PLL significantly varies with pH changes around pH = 7,[27] which may negatively impact FET sensitivity. This is because ψ_0 was pinned by the pH-sensitive surface group, referred to as a negative pH interference

mechanism.[30] Consequently, in FET biosensors, biosensitivity is inversely related to pH sensitivity.[31] As our devices were modified with the quaternary ammonium cation, it is expected that the pH interference mechanism is relatively suppressed, which also contributes to the signal enhancements.

In this study, a simple decoration process, i.e., physisorption, was used to develop the devices, aiming to prove the concept of the SCM-GFETs. Although the developed GFETs specifically detected the target as they were designed to achieve a near-zero surface potential and low pH sensitivity through the decoration, the resulting ψ_0 (or ζ-potential) value of the devices remains to be assessed. Consequently, there is the potential for further signal enhancement through the optimization of ψ_0. The charges of the blocking molecules and capture probes also affected the surface charge of the GFETs. In addition to the surface charges, the density of the antibody also affects the signal, which may be improved by using linker molecules such as PBASE.[10,13] Moreover, the charges of the analyte may also affect the surface charge when the analyte concentration is high. Thus, the design and optimization of the surface charge of GFETs must be tailored to match specific target applications, which will be the focus of future research.

5. CONCLUSIONS

We demonstrated CRP sensing using SCM-GFETs. An array of SCM-GFETs functionalized with anti-CRP mAb and nonfunctionalized GFETs was integrated onto a chip, and differential measurements were performed to eliminate background changes and improve the measurement reliability. The FET response was consistent with the fluorescence images, which showed specific adsorption onto the anti-CRP mAb. Additionally, the estimated K_D agreed with a previously reported value, providing further support that the results were attributed to the specific adsorption of CRP. In contrast, signals from GFETs without decoration were buried in the noise because of nonlinear electrolytic screening, highlighting the significance of surface-charge modulation. The LOD of the system was estimated to be 2.9 nM, which can be improved through further optimization of the surface charges to match the target applications. In FET biosensors, charge screening in an electrolyte solution remains a major limiting factor for sensitivity, thereby restricting the application window for FET sensors. Our approach can pave the way for further applications of GFET biosensors.

ASSOCIATED CONTENT

Ⓢ Supporting Information

The Supporting Information is available free of charge at https://pubs.acs.org/doi/10.1021/acsomega.3c07650.

> Binding kinetics measured by using biolayer interferometry; overview of the custom-built portable measurement system; histograms of $V_{DP,sig}$ and $V_{DP,ref}$; optical images of GFETs after the incubation of NR_3^+ and COOH PS bead suspensions; time series of the mean ΔV_{DP} and the data points in the last 10 min at each step in Figure 3b; fluorescence images of GFETs; schematic of nonantibody immobilized GFETs and the response; fluorescence images of anti-CRP and QACs modified sample and QACs modified sample; and optical images of GFETs$_{sig}$ after the experiments in Figure 3 (PDF)

AUTHOR INFORMATION

Corresponding Author

Shota Ushiba − *Murata Manufacturing Co., Ltd., Kyoto 617-8555, Japan;* ⓞ orcid.org/0000-0001-7652-081X; Email: shota.ushiba@murata.com

Authors

Tomomi Nakano − *Murata Manufacturing Co., Ltd., Kyoto 617-8555, Japan*

Ayumi Shinagawa − *Murata Manufacturing Co., Ltd., Kyoto 617-8555, Japan*

Naruto Miyakawa − *Murata Manufacturing Co., Ltd., Kyoto 617-8555, Japan*

Tadashi Kato − *Murata Manufacturing Co., Ltd., Kyoto 617-8555, Japan*

Katsuyuki Yofu − *Murata Manufacturing Co., Ltd., Kyoto 617-8555, Japan*

Takao Ono − *Osaka University, Ibaraki, Osaka 567-0047, Japan;* ⓞ orcid.org/0000-0002-6717-123X

Yasushi Kanai − *International Center for Synchrotron Radiation Innovation Smart, Tohoku University, Sendai 980-8577, Japan*

Shinsuke Tani − *Murata Manufacturing Co., Ltd., Kyoto 617-8555, Japan*

Masahiko Kimura − *Murata Manufacturing Co., Ltd., Kyoto 617-8555, Japan*

Kazuhiko Matsumoto − *Osaka University, Ibaraki, Osaka 567-0047, Japan*

Complete contact information is available at:
https://pubs.acs.org/10.1021/acsomega.3c07650

Author Contributions

S.U., T.N., and A.S. conducted device fabrication and electrical measurements. T.K. developed the custom-built portable measurement systems. S.U., T.N., A.S., N.M., S.T., M.K., and K.M. planned the project. M.K. and K.M. supervised the study. All authors have discussed the results and contributed to the preparation of the manuscript. All authors approved the final version of the manuscript.

Notes

The authors declare no competing financial interest.

REFERENCES

(1) Bhattacharyya, I. M.; Shalev, G. Electrostatically governed debye screening length at the solution-solid interface for biosensing applications. *ACS Sens.* **2020**, *5* (1), 154.

(2) Liu, Y.; Dutton, R. W. Effects of charge screening and surface properties on signal transduction in field effect nanowire biosensors. *J. Appl. Phys.* **2009**, *106* (1), No. 014701.

(3) Gupta, M.; Santermans, S.; Hellings, G.; Lagae, L.; Martens, K.; Van Roy, W. Surface charge modulation and reduction of non-linear electrolytic screening in FET-based biosensing. *IEEE Sensors J.* **2021**, *21* (4), 4143.

(4) Wunderlich, B. K.; Neff, P. A.; Bausch, A. R. Mechanism and sensitivity of the intrinsic charge detection of biomolecular interactions by field effect devices. *Appl. Phys. Lett.* **2007**, *91* (8), No. 083904.

(5) Shoorideh, K.; Chui, C. O. Optimization of the sensitivity of FET-based biosensors via biasing and surface charge engineering, *IEEE Trans. Electron Devices* **2012**, *59* (11), 3104.

(6) Hwang, E. H.; Adam, S.; Das Sarma, S. D. Carrier transport in two-dimensional graphene layers. *Phys. Rev. Lett.* **2007**, *98* (18), No. 186806.

(7) Bolotin, K. I.; Sikes, K. J.; Jiang, Z.; Klima, M.; Fudenberg, G.; Hone, J.; Kim, P.; Stormer, H. L. Ultrahigh electron mobility in suspended graphene. *Solid State Commun.* **2008**, *146* (9−10), 351.

(8) Paulus, G. L. C.; Nelson, J. T.; Lee, K. Y.; Wang, Q. H.; Reuel, N. F.; Grassbaugh, B. R.; Kruss, S.; Landry, M. P.; Kang, J. W.; Vander Ende, E.; Zhang, J.; Mu, B.; Dasari, R. R.; Opel, C. F.; Wittrup, K. D.; Strano, M. S. A graphene-based physiometer array for the analysis of single biological cells. *Sci. Rep.* **2014**, *4*, 1.

(9) Ushiba, S.; Ono, T.; Kanai, Y.; Inoue, K.; Kimura, M.; Matsumoto, K. Graphene as an imaging platform of charged molecules. *ACS Omega* **2018**, *3* (3), 3137.

(10) Andoy, N. M.; Filipiak, M. S.; Vetter, D.; Gutiérrez-Sanz, Ó; Tarasov, A. Graphene-based electronic immunosensor with femto-molar detection limit in whole serum. *Adv. Mater. Technol.* **2018**, *3* (12), No. 1800186.

(11) Kanai, Y.; Ohmuro-Matsuyama, Y.; Tanioku, M.; Ushiba, S.; Ono, T.; Inoue, K.; Kitaguchi, T.; Kimura, M.; Ueda, H.; Matsumoto, K. Graphene field effect transistor-based immunosensor for ultra-sensitive noncompetitive detection of small antigens. *ACS Sens.* **2020**, *5* (1), 24.

(12) Ramadan, S.; Lobo, R.; Zhang, Y.; Xu, L.; Shaforost, O.; Tsang, Kwong Hong; D, K H; Feng, J.; Yin, T.; Qiao, M.; Rajeshirke, A.; Jiao, L. R.; Petrov, P. K.; Dunlop, I. E.; Titirici, M. M.; Klein, N Carbon-dot-enhanced graphene field-effect transistors for ultrasensitive detection of exosomes. *ACS Appl. Mater. Interfaces* **2021**, *13* (7), 7854.

(13) Seo, G.; Lee, G.; Kim, M. J.; Baek, S. H.; Choi, M.; Ku, K. B.; Lee, C. S.; Jun, S.; Park, D.; Kim, H. G.; Kim, S. J.; Lee, J. O.; Kim, B. T.; Park, E. C.; Kim, S. Il. Rapid detection of COVID-19 causative virus (SARS-CoV-2) in human nasopharyngeal swab specimens using field-effect transistor-based biosensor. *ACS Nano* **2020**, *14* (4), 5135.

(14) Bepete, G.; Anglaret, E.; Ortolani, L.; Morandi, V.; Huang, K.; Pénicaud, A.; Drummond, C. Surfactant-free single-layer graphene in water. *Nat. Chem.* **2017**, *9* (4), 347.

(15) Zuccaro, L.; Krieg, J.; Desideri, A.; Kern, K.; Balasubramanian, K. Tuning the isoelectric point of graphene by electrochemical functionalization. *Sci. Rep.* **2015**, *5*, 11794.

(16) Lau, A. C.; Furlong, D. N.; Healy, T. W.; Grieser, F. The electrokinetic properties of carbon black and graphitized carbon black aqueous colloids. *Colloids Surf.* **1986**, *18* (1), 93.

(17) Ushiba, S.; Okino, T.; Miyakawa, N.; Ono, T.; Shinagawa, A.; Kanai, Y.; Inoue, K.; Takahashi, K.; Kimura, M.; Matsumoto, K. State-space modeling for dynamic response of graphene FET biosensors. *Jpn. J. Appl. Phys.* **2020**, *59* (SG), SGGH04.

(18) Miyakawa, N.; Shinagawa, A.; Kajiwara, Y.; Ushiba, S.; Ono, T.; Kanai, Y.; Tani, S.; Kimura, M.; Matsumoto, K. Drift suppression of solution-gated graphene field-effect transistors by cation doping for sensing platforms. *Sensors (Basel)* **2021**, *21* (22), 7455.

(19) Ushiba, S.; Nakano, T.; Miyakawa, N.; Shinagawa, A.; Ono, T.; Kanai, Y.; Tani, S.; Kimura, M.; Matsumoto, K. Robust graphene field-effect transistor biosensors via hydrophobization of SiO_2 substrates. *Appl. Phys. Exp.* **2022**, *15* (11), 115002.

(20) Ushiba, S.; Miyakawa, N.; Ito, N.; Shinagawa, A.; Nakano, T.; Okino, T.; Sato, H. K.; Oka, Y.; Nishio, M.; Ono, T.; Kanai, Y.; Innami, S.; Tani, S.; Kimuara, M.; Matstumoto, K. Deep-learning-based semantic image segmentation of graphene field-effect transistors. *Appl. Phys. Exp.* **2021**, *14* (3), No. 036504.

(21) Brooks, S.; Gelman, A.; Jones, G. L.; Meng, X.-L. *Handbook of Markov Chain Monte Carlo*; Chapman & Hall/CRC: New York, 2011.

(22) Vashist, S. K.; Venkatesh, A. G.; Marion Schneider, E.; Beaudoin, C.; Luppa, P. B.; Luong, J. H. Bioanalytical advances in assays for C-reactive protein. *Biotechnol. Adv.* **2016**, *34* (3), 272.

(23) Salihoglu, O.; Kakenov, N.; Balci, O.; Balci, S.; Kocabas, C. Graphene as a reversible and spectrally selective fluorescence quencher. *Sci. Rep.* **2016**, *6*, 33911.

(24) Gao, N.; Gao, T.; Yang, X.; Dai, X.; Zhou, W.; Zhang, A.; Lieber, C. M. Specific detection of biomolecules in physiological solutions using graphene transistor biosensors. *Proc. Natl Acad. Sci. U. S. A.* **2016**, *113* (51), 14633.

(25) Oka, Y.; Ushiba, S.; Miyakawa, N.; Nishio, M.; Ono, T.; Kanai, Y.; Watanabe, Y.; Tani, S.; Kimura, M.; Matsumoto, K. Ionic strength-sensitive and pH-insensitive interactions between C-reactive protein (CRP) and an anti-CRP antibody. *Biophys. Physicobiol.* **2022**, *19*, No. e190003.

(26) Correia, J.; Oliveira, F. R.; De Cassia Siqueira Curto Valle, R; Valle, J. A. B Preparation of cationic cotton through reaction with different polyelectrolytes. *Cellulose (Lond)* **2021**, *28* (18), 11679.

(27) Naassaoui, I.; Aschi, A. Evaluation of properties and structural transitions of poly-L-lysine: effects of pH and temperature. *J. Macromol. Sci. B* **2019**, *58* (8), 673.

(28) Chu, Y.; Gao, Y.; Tang, W.; Qiang, L.; Han, Y.; Gao, J.; Zhang, Y.; Liu, H.; Han, L. Attomolar-level ultrasensitive and multiplex microRNA detection enabled by a nanomaterial locally assembled microfluidic biochip for cancer diagnosis. *Anal. Chem.* **2021**, *93* (12), 5129.

(29) Gao, J.; Wang, C.; Wang, C.; Chu, Y.; Wang, S.; Sun, M; Ji, H.; Gao, Y.; Wang, Y.; Han, Y.; Song, F.; Liu, H.; Zhang, Y.; Han, L. Poly-l-lysine-modified graphene field-effect transistor biosensors for ultrasensitive breast cancer miRNAs and SARS-CoV-2 RNA detection. *Anal. Chem.* **2022**, *94* (3), 1626.

(30) Santermans, S.; Schanovsky, F.; Gupta, M.; Hellings, G.; Heyns, M.; Van Roy, W.; Martens, K. The significance of nonlinear screening and the PH interference mechanism in field-effect transistor molecular sensors. *ACS Sens.* **2021**, *6* (3), 1049.

(31) Kumar, N.; Kumar, S.; Kumar, J.; Panda, S. Investigation of mechanisms involved in the enhanced label free detection of prostate cancer biomarkers using field effect devices. *J. Electrochem. Soc.* **2017**, *164* (9), B409.